RSC Advances

PAPER

View Article Online
View Journal | View Issue

Cite this: *RSC Adv.*, 2025, **15**, 39795

Synergistic g-C_3N_4@SnO_2 nano heterostructures and their application for enhanced humidity sensing

Priyanka Birla, [a] Manish Shinde, *[a] Shweta Jagtap, [b] Sudhir Arbuj, [a] Sunit Rane *[a] and Bharat Kale [ac]

Received 13th August 2025
Accepted 3rd October 2025

DOI: 10.1039/d5ra05966f

rsc.li/rsc-advances

We report g-C_3N_4@SnO_2 nanocomposites as efficient humidity-sensing materials. SnO_2 nanoparticles synthesized *via* a facile solvothermal route were coupled *in situ* with g-C_3N_4 sheets through an economic solid-state process. XRD, FTIR, and XPS confirmed the tetragonal SnO_2 phase and successful composite formation, while FESEM and FETEM showed 20–50 nm SnO_2 nanoparticles anchored on g-C_3N_4. The composites exhibited a red-shifted optical absorption edge and suppressed photoluminescence, indicating enhanced charge separation. The sensors, fabricated by screen printing, exhibited stable operation in the 20–80% RH range. Humidity-sensing studies revealed outstanding performance for the 15 wt% g-C_3N_4@SnO_2 composite, with a sensitivity of 20.2 Ω/%RH as well as rapid response (25 s) and recovery (45 s) times. These results establish g-C_3N_4@SnO_2 as a promising platform for next-generation, ultrasensitive and fast-response humidity sensors.

Introduction

Artificial intelligence-based machines, devices and components have gained importance in the modern era; sensors play a vital role in such development. Among various sensors being developed, humidity sensors are crucial but have received relatively little attention. Humidity is the presence of water vapour in the atmosphere, and hence influences various physical, chemical, and biological processes.[1]

Humidity sensing and measurement is very crucial in industries as humid environments can disturb all categories of commercial setups, like in agriculture and the food industry (crop protection (dew prevention) and soil relative humidity monitoring), healthcare and pharmaceutical industry (respiratory equipment, sterilizers, incubators), electronics, printing, food, construction *etc.*, which could hamper the cost, quality, health, and safety of the product and therefore a trustworthy, steady, repeatable, and economic method for humidity measurement is needed as humidity can be considered/measured in numerous ways.[2–4]

Diversiform humidity sensors with different sensing mechanisms have been reported, including resistive, impedance, capacitive, quartz crystal microbalance (QCM), surface acoustic wave (SAW), field-effect transistor (FET), and optical fibre humidity sensors.[2] However, resistive humidity sensors have advantages over all the aforementioned humidity sensors owing to their cost-effective fabrication, easy integrability with complementary metal oxide semiconductor (CMOS) platforms, and easy and efficient operation.[5] In this field, researchers are continually searching for ways to develop humidity-sensing materials that have good stability, long-term durability, rapid response and recovery time, high linearity, and exceptionally low hysteresis.

To date, many researchers have worked on various kinds of strategies[6] and materials *viz.*, vanadates[7] metal sulfides (*e.g.*, *n*-WS_2),[8] MXenes,[9] perovskite materials,[10] a variety of conjugated polymers,[11] 2D rGO/2D MoS_2 [12] and chitosan/zinc oxide/single-walled carbon nanotubes.[13] Additionally, materials such as Al_2O_3,[14] SiO_2,[15] perovskites (ABO_3),[16] spinel (AB_2O_4), and semiconductor metal oxides, such as ZnO,[17,18] SnO_2,[19,20] TiO_2,[21,22] CuO,[23] and WO_3,[24,25] are broadly studied for humidity sensing.

Graphitic carbon nitride proves its supremacy owing to various fascinating qualities like large density of active sites, decent semiconducting nature and 2D polymeric sheet-like structure, which combine to give a large specific surface area and enhanced electric conductivity through superior electron transport, making it responsive to the adsorption of water molecules and an apt candidate for humidity sensing.[26,27] So far, there is a solitary report on the use of pure g-C_3N_4 for humidity sensing.[28]

SnO_2 is one of the abundantly available n-type metal oxides with exceptional electrochemical stability and low production cost, good porosity and huge surface area (for nanoscale SnO_2),

[a]*Centre for Materials for Electronics Technology, Off Pashan Road, Panchwati, Pune-411008, India. E-mail: sunit@cmet.gov.in; manish@cmet.gov.in*

[b]*Department of Electronic and Instrumentation Science, Savitribai Phule Pune University, Pune-411007, India*

[c]*Material Science Department, MIT World Peace University (MITWPU), Paud Road, Pune-411038, India*

offering more active sites for the surface chemical interaction and proving its suitability for humidity-sensing practical applications, but it exhibits a narrow range and a long response/recovery time.[29–31] Some of these issues can be addressed by combining SnO_2 with other metals/metal oxides and carbon-based materials as dopants or composites, as they offer good thermal and chemical stability, exceptional electronic band structure, decent electrical behavior, *etc.*[32]

The composite system of SnO_2 with g-C_3N_4 is expected to provide such a synergistic effect in the humidity-sensing studies due to the high surface area, conducting nature, and stability of g-C_3N_4. Individually, SnO_2-based composites with different materials, as well as g-C_3N_4-based composites with various materials, have been reported as humidity sensors.[33] To the best of our knowledge, no such reports are available where a g-C_3N_4@SnO_2 composite system was explored for humidity-sensing applications.

In this context, we synthesized g-C_3N_4@SnO_2 nanocomposites with different wt% ratios of g-C_3N_4 and SnO_2 using a facile solid-state method. The humidity-sensing properties, including response time and sensitivity, of g-C_3N_4@SnO_2 were investigated with respect to change in wt% composition.

Experimental

Materials and methods

For material synthesis, analytical-grade tin chloride (Otto Chemicals), melamine (Sigma Aldrich), isopropanol (IPA, SD Fine chemicals) and NaOH (Qualigen) were procured and used without further purification.

Synthesis of pristine nanostructured tin oxide was accomplished by solvothermal method using $SnCl_4 \cdot 5H_2O$ as the metal precursor. In a typical process, 0.02 M of tin precursor was dissolved in a mixture of solvents, namely, IPA and distilled water in the volume ratio of 4 : 1. On complete dissolution, a strong base solution (2 M NaOH in water) was added to adjust the pH to 12. This solution was then transferred to a Teflon container, packed in a stainless steel autoclave and heated at 150 °C for 24 h (Fig. 1). After hydrothermal treatment, the resultant precipitate was washed several times until neutral pH was achieved, then filtered and dried at 60 °C. For synthesis of g-C_3N_4, we used melamine as the precusor which was heated at 550 °C for 2 h with ramp rate of 5 °C min^{-1} using a facile solid state method. g-C_3N_4@SnO_2 nanocomposites with different wt% ratios of g-C_3N_4 and SnO_2 were prepared using the same protocol (Table 1).

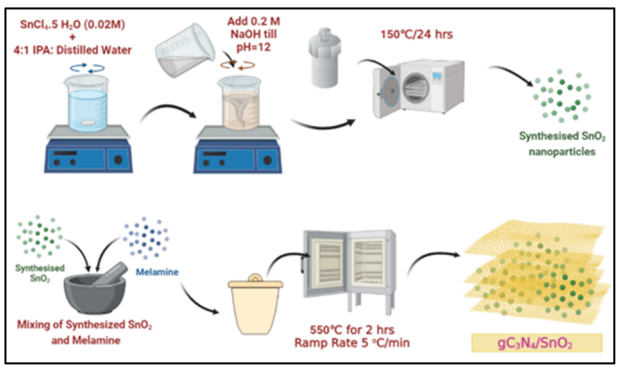

Fig. 1 Schematic representation of the preparation of g-C_3N_4@SnO_2 nanostructures.

Table 1 Wt% composition of precursors for preparation of g-C_3N_4@SnO_2 nanostructures

Sr. no.	Composition (wt%)	SnO_2 (in grams)	Melamine (in grams)
1	5	1.5 g	0.16
2	10		0.33
3	15		0.5
4	20		0.66

Characterization

X-ray diffraction (XRD) analysis was carried out using a Rigaku MiniFlex 600 diffractometer with Cu Kα1 radiation ($\lambda = 1.5406$ Å) and a step size of 0.02 in the 2θ range of 20–80°. XRD refinement analysis was done using MAUD software. Diffuse reflectance UV-vis spectra were recorded in the 200–800 nm range using a Shimadzu spectrophotometer (UV 3600). FT-IR spectra were taken on an IRAffinity-1S 01130 Shimadzu spectrometer over the range of 400–4000 cm^{-1}. The surface area of the samples was determined with the Brunauer–Emmett–Teller (BET) method using a Quantachrome NOVA touch LX1. X-ray photoelectron spectroscopy (XPS) study was conducted to determine the elemental composition using a PHI Versa Probe. The surface morphology and elemental composition of the nanostructures were analyzed using scanning electron microscopy (SEM) and field emission transmission electron microscopy (FETEM) using JEOL models JSM6360A and JEM 2200FS, respectively.

Humidity sensor film fabrication

g-C_3N_4/SnO_2 composite powders were uniformly blended with terpinol to formulate the functional material paste, followed by screen-printing technique for subsequent deposition onto the glass substrate. Prepared films were then dried under an IR lamp. For resistivity measurement, ohmic contacts were made using imported silver paint (RS Components UK).

Humidity measurements setup

For humidity measurement, an in-house enclosed system was employed, consisting of an enclosed glass dome with a rubber cork to maintain an airtight environment for uniform moisture distribution and a Hanna Instruments (HI 9565) humidity meter (range: 20–95% RH, accuracy: ±3% RH) as shown in Fig. 2. All measurements were conducted at room temperature, and an enclosed system ensured that the air concentration remained constant throughout the experiments. Both the humidity probe and substrate holder were positioned at the center point of this enclosed humidity measurement setup. A dehumidifier based on phosphorous pentoxide was employed

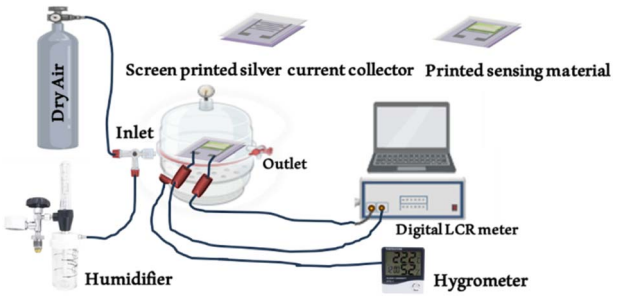

Fig. 2 Schematic representation of % relative humidity measurement setup.

for the sake of humidity reduction. The humidity-sensing measurements were gathered across 20% to 80% RH and variations in humidity were carefully monitored as a function of change in resistance at room temperature, *i.e.*, 25 °C, which was maintained using the air conditioner in the room. A standard humidity meter along with a precise digital multimeter was used for reference.

Impedance response of humidity sensors

Electrochemical impedance spectroscopy (EIS) analysis of the 15% g-C_3N_4@SnO_2 humidity sensor in the frequency range of 10 Hz to 8 MHz was carried out using an LCR meter HIOKI IM 3536. The sensor was connected to the dewpoint hygrometer HI9565 for humidity monitoring. After establishing the desired humidity value, the impedance, resistance, capacitance, *etc.* were measured. Resistance transients were measured by assessing the sensor's resistance change when alternately exposed to two controlled humidity chambers. While impedance spectra helped assess overall electrical properties, resistance was selected for transient studies as it offers a simpler and more direct way to follow real-time adsorption and desorption. The resistance was recorded using a Tektronix 4040 multimeter and plotted as transient curves. From these, the response and recovery times were calculated as the duration needed to reach 90% of the total resistance change.

Results and discussion

X-ray diffraction analysis

The crystallinity and phase purity of the prepared samples were studied using XRD and the results are presented in Fig. 3a. XRD pattern for pristine SnO_2 sample showed Bragg's diffraction peaks at 2θ values of 26.80, 33.92, 37.97, 38.85, 51.87, 54.68, 58.02, 61.86, 65.03, 66.07, 71.43 and 78.62° which were assigned to (110), (101), (200), (111), (211), (220), (002), (310), (112), (301), (202) and (321) planes of tetragonal phase corresponding to JCPDS no. 88-0287. XRD pattern of g-C_3N_4 (JCPDS card no. 087-15260) presented two diffraction characteristic peaks, first around 13.0°, which confirmed (100) lattice plane of triazine units, whereas the (002) lattice plane, confirming interlayer stacking of aromatic segments, was observed as a high intensity peak around 27.3°. All the characteristic peaks of SnO_2 were

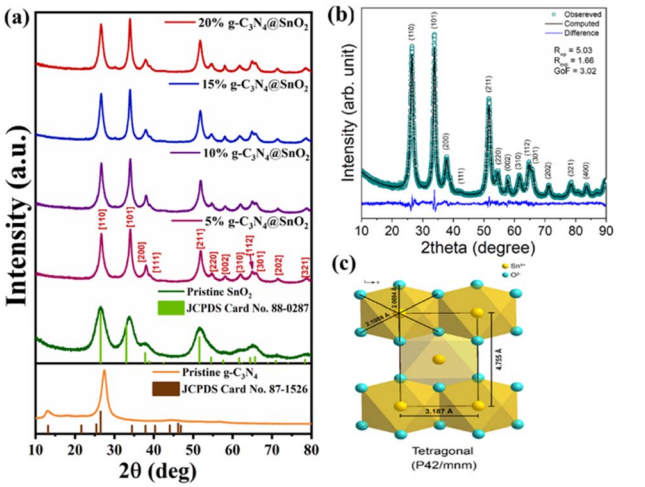

Fig. 3 (a) X-ray diffractograms of prepared pristine g-C_3N_4, SnO_2, and g-C_3N_4@SnO_2 nanocomposites and crystal structure refinement analysis of the g-C_3N_4@SnO_2 nanocomposite sample. (b) Comparison between the observed and computed XRD patterns and (c) tetragonal (space group $P4_2/mnm$) crystal structure of the SnO_2 lattice.

observed in the XRD patterns of the g-C_3N_4@SnO_2 nanocomposite samples.

The significant diffraction peaks for g-C_3N_4 were not observed in the XRD patterns of the nanocomposites prepared with g-C_3N_4@SnO_2, which is obviously due to the grain growth of SnO_2 owing to annealing in the solid-state reaction step and the g-C_3N_4 peaks around 27.3° might be covered by the significantly higher intensity characteristic peak of SnO_2 at 26.8°.[34,35]

Fig. 3b shows the Rietveld XRD refinement analysis results for the 15% g-C_3N_4@ SnO_2 sample carried out by MAUD software. The tetragonal (space group: $P4_2/mnm$) unit cell of SnO_2 lattice and two types of Sn–O bond lengths with values of 2.1088 Å and 2.0694 Å were calculated within the SnO_6 octahedra, as indicated in Fig. 3b and c, respectively.

UV-DRS spectroscopy

Optical properties of the prepared g-C_3N_4@SnO_2 nanocomposites were recorded by UV-DRS spectroscopy, as shown in Fig. 4a and b. The pristine g-C_3N_4 and SnO_2 showed absorption edges at 470 and 365 nm, respectively (Fig. 4a). In the case of the nanocomposites, with increasing g-C_3N_4 loading, the major coupling interaction between SnO_2 and g-C_3N_4 red-shifted the absorption band edge from the UV region to visible, from 365 to 420 nm.[35]

The band gap values of pristine g-C_3N_4 and SnO_2 were calculated to be 2.77 eV and 3.69 eV, respectively (Fig. 4b). For the 5, 10, 15 and 20 wt% g-C_3N_4@SnO_2 nanocomposites, the band gap energy values calculated using the Kubelka–Munk equation were in the range of 3.54–3.33 eV. The decrease in the band gap designated the formation of the composite, which affected the energy levels in the band structure of SnO_2 by generating imperfections on the surface of the nanocomposites, making them suitable for humidity sensing.[36]

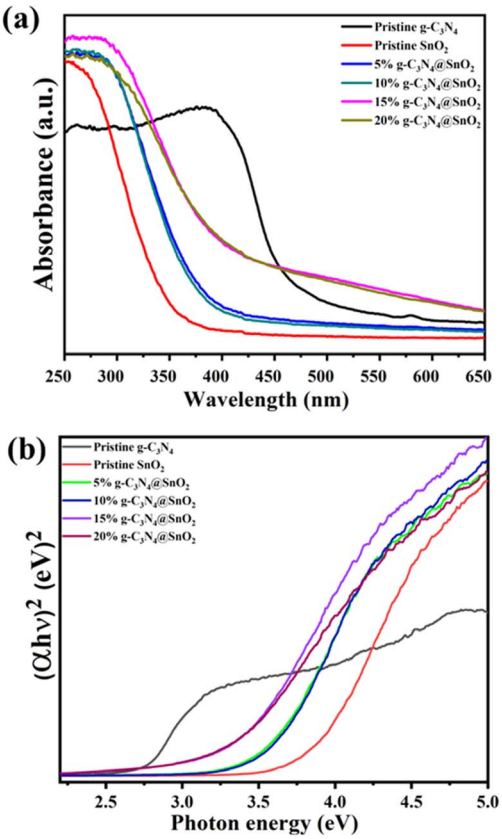

Fig. 4 (a) UV-DRS spectra and (b) Tauc plot of pristine g-C_3N_4, pristine SnO_2, and the prepared g-C_3N_4@SnO_2 nanocomposites.

Photoluminescence spectroscopy

Photoluminescence spectroscopy was used to analyze the recombination efficiency of the photogenerated charge carriers. Fig. 5 shows the room-temperature PL spectra with emission wavelength of 300 nm for the g-C_3N_4, SnO_2 and different wt% g-C_3N_4@SnO_2 nanocomposites. The pristine g-C_3N_4 sample displayed a strong emission band at 448 nm. For pristine SnO_2 and the g-C_3N_4@SnO_2 composites, three emission bands were observed, the first strong band around 363 nm might be due to the interstitial transition of Sn species and their respective oxygen vacancy, while the two small peaks in the visible region at 415 and 468 nm hint at the radiative recombination of the electron from the oxygen vacancy created due to Sn species with the holes.[37]

The PL peak intensities of different wt% g-C_3N_4@SnO_2 nanocomposites were relatively lower than those of the pristine samples, which signified the reduction of the electron–hole pairs recombination efficiency and increased with respect to wt% loading of g-C_3N_4 as a result of the strong interactive coupling of the oxygen vacancy present in SnO_2 with the g-C_3N_4 sheets, which led to a decrease in trap density and progressive carrier mobility resulting in a higher PL intensity.[35,36,38]

FTIR spectroscopy

FTIR spectra (Fig. 6) were obtained to analyze the chemical structures of the samples. Typical vibration peaks observed at 880, 1215, 1403, 1410, 1550, and 1630 cm^{-1} corresponded to the distinguishing stretching vibration modes of g-C_3N_4. The amino group present in g-C_3N_4 *i.e.* N–H and the hydroxyl group (–OH) from SnO_2 on the surface displayed broad stretching vibration band in the same range of 3000–3500 cm^{-1}. The peak at 880 cm^{-1} were assigned to the triazine units, and the stretching vibrations at 1255 to 1550 cm^{-1} confirmed the presence of the C–N heterocyclic structure in the g-C_3N_4 sheets. The C–N mode was reflected at 1309 cm^{-1} in pristine g-C_3N_4.[36]

The sharp absorption peaks at 498 and 476 cm^{-1} were fitted to the anti-symmetrical stretching vibration of Sn–O–Sn in the pristine SnO_2 and the 15 wt% g-C_3N_4@SnO_2 composite, respectively. Vibrational properties of the triazine ring of g-C_3N_4 were reflected around 880 and 1630 (C=N stretching) cm^{-1}

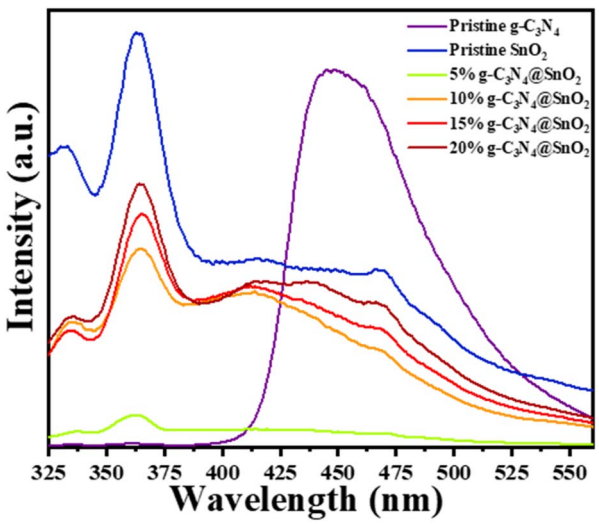

Fig. 5 Photoluminescence spectra of pristine g-C_3N_4, pristine SnO_2, and the prepared g-C_3N_4@SnO_2 composite powders.

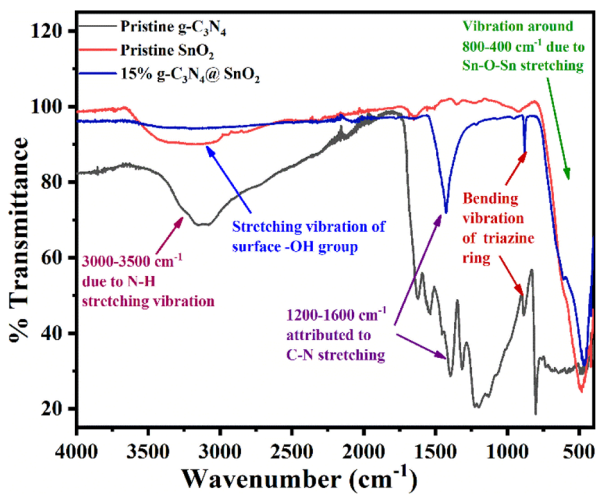

Fig. 6 FTIR spectra of pristine g-C_3N_4, pristine SnO_2, and prepared 15 wt% g-C_3N_4@SnO_2 composite powders.

whereas for the 15 wt% g-C_3N_4@SnO_2 composite, these stretching vibrations were noted around 885 and 1649 cm^{-1}, which implied an interaction between the g-C_3N_4 sheets and the SnO_2 particles, confirming composite formation. FTIR spectra of pristine g-C_3N_4, SnO_2, and different wt% g-C_3N_4@SnO_2 composites provided in the SI Fig. S1 revealed peak positions similar to those of the 15wt% g-C_3N_4@SnO_2 composite powder.[35]

X-ray photoelectron spectroscopy

Information pertaining to the chemical bonding states, compositions and heterojunctions was obtained by XPS and the results are displayed in Fig. S2 and 7. The survey spectra (Fig. S2) revealed the existence of Sn, O, C and N elements in the 15 wt% g-C_3N_4@SnO_2 sample.[34]

For Sn 3d XPS spectrum (Fig. 7a), the characteristic peaks at 486.2 eV and 494.7 eV were assigned to Sn $3d_{5/2}$ and Sn $3d_{3/2}$, having an energy difference of 8.5 eV, which conferred the presence of the Sn^{4+} oxidation state in the Sn–O bond instead of Sn^{2+} or Sn0 state whereas the peak around 496.6 was referred to as a satellite peak. The binding energy peaks due to Sn are reported at 486.0 eV and 494.4 eV, implying a difference of 0.2 eV from the values obtained in our case, suggesting the formation of the g-C_3N_4@SnO_2 heterojunction. Interface interaction at such a heterojunction could result in the weak transfer of charges from the g-C_3N_4 nanosheets to the SnO_2 nanostructures.[38–40] The O 1s XPS spectra in Fig. 7b show that three contributions were separated out: the first peak at 530.22 eV describing SnO_2 lattice oxygen, the second peak at 531.6 eV assigned to oxygen in defect states, and the third one at 535.3 eV for oxygen from –OH groups on the sample surface.[35,41,42]

The high-resolution C 1s XPS spectrum of 15 wt% g-C_3N_4@SnO_2 sample in Fig. 7c can be decomposed into two peaks at 284.52 eV and 288.23 eV, ascribed to sp^2 hybridized carbon in C=C/C–C and N–C=N, respectively. Moreover, the high-resolution N 1s XPS spectrum of the sample (Fig. 7d) exhibited three binding energy peaks at 398.0 eV, 399.3 eV and 400.4 eV, corresponding to sp^2-hybridized nitrogen (C=N–C), tertiary graphite nitrogen (N–C3) and amino (C–N–H), respectively.[30,35] Thus, XPS spectra revealed the creation of a g-C_3N_4@SnO_2 heterojunction.

FESEM imaging

Fig. 8 depicts the surface morphology of the pristine g-C_3N_4, pristine SnO_2 and different wt% g-C_3N_4@SnO_2 nanocomposites studied using field emission scanning electron microscopy (FESEM). Fig. 8a and b presents a clear agglomerated multi-layered structure corresponding to pristine g-C_3N_4. Fig. 8c and d, for the pristine SnO_2 micro-nanopowder, shows a mixture of submicron to nanoscale particles having multi-shaped forms *viz.* spheres, cubes, rods and occasionally microscale spherical morphology having particle sizes in the range of 2–3 μm composed of agglomerated 20–50 nm sized particles. FESEM images of the different wt% g-C_3N_4@SnO_2 composites revealed that SnO_2 particles distributed onto the surface of g-C_3N_4 sheets prepared with variations of the g-C_3N_4 composition as 5 (Fig. 8 e and f), 10 (Fig. 8 g and h), 15 (Fig. 8 i and j) and 20 (Fig. 8 k and l) wt%.

FETEM imaging

FETEM images for the 15 wt% g-C_3N_4@SnO_2 composite powder are shown in Fig. 9. The FETEM images at low and intermediate magnification (Fig. 9a–c) display agglomerated bunches of submicrons to nanoscale particles embedded in g-C_3N_4 sheets. The agglomerated bunches are made up of spherical, rod and cube-like morphologies of sizes in the range of 20–50 nm. The apparent ambiguity between FESEM and FETEM images arises from the difference in resolution and imaging depth between FETEM (which captures the internal structure at the nanoscale) and FESEM (which emphasizes surface topography at the micro- and nano-scale). However, both techniques provided

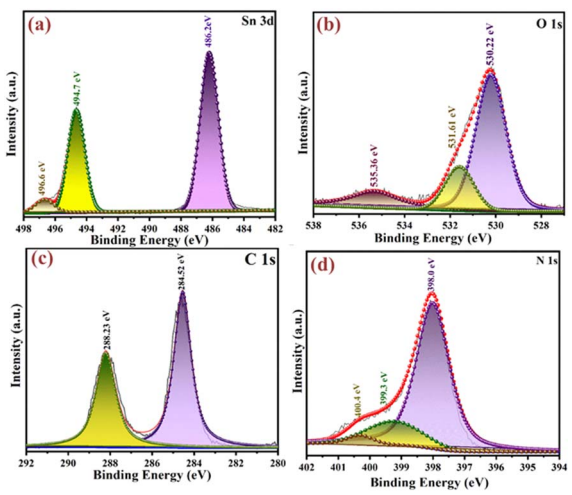

Fig. 7 XPS spectra of prepared 15 wt% g-C_3N_4@SnO_2 nanocomposite corresponding to the elements (a) Sn 3d, (b) O 1s, (c) C 1s and (d) N 1s.

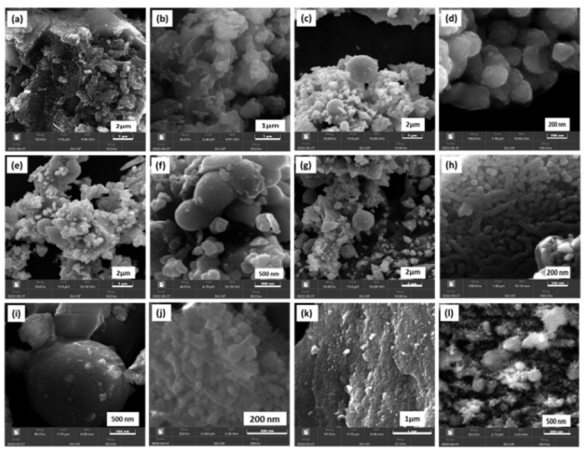

Fig. 8 FESEM images of pristine g-C_3N_4 (a and b), pristine SnO_2 (c and d) and 5 (e and f), 10 (g and h), 15 (i and j) and 20 (k and l) wt% g-C_3N_4@SnO_2 nanocomposites at low and high magnifications, respectively.

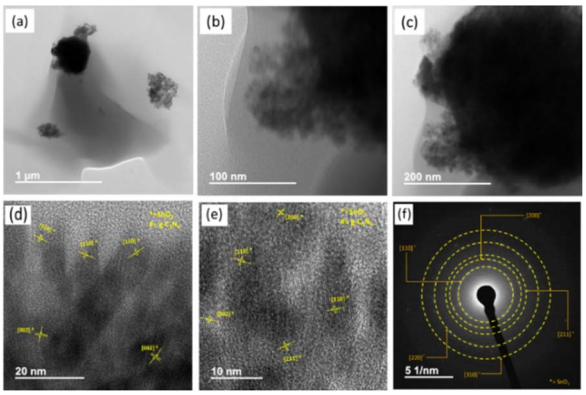

Fig. 9 FETEM images of prepared 15 wt% g-C_3N_4@SnO_2 nanostructures at (a), (b) low, (c) intermediate, (d), and (e) high magnifications and (f) SAED pattern.

similar morphological information. Validation of the almost analogous microstructural traits of SnO_2 particles on g-C_3N_4 sheets was done by providing more such FETEM images in SI Fig. S3. In high-resolution images (Fig. 9d and e), fringes for SnO_2 nanoparticles, with lattice spacing of 3.74, 2.53 and 1.94 Å ascribable to (110), (200) and (211) planes, corresponding to its tetragonal phase were noticed whereas g-C_3N_4 sheets confirmed the lattice spacing value of 3.68 Å annotated to the (002) plane. The selected area electron diffraction (SAED) pattern (Fig. 9f) for the 15 wt% g-C_3N_4@SnO_2 composite evinced the intermittent ring structures displaying regular bright spots.[38]

The distribution of elements in the 15 wt% g-C_3N_4@SnO_2 composite sample was ascertained using the FETEM-STEM-EDS-elemental mapping mode and the results are shown in Fig. 10. The electron image (Fig. 10a) and elemental mapping images accountable to Sn and O (Fig. 10b and c, respectively) correlated well with each other while in case of g-C_3N_4, it was annotated that elemental mapping images for C and N also (Fig. 10d and e) overlayed each other in such a manner that SnO_2 nanoparticles were positioned on the sheet-like structure

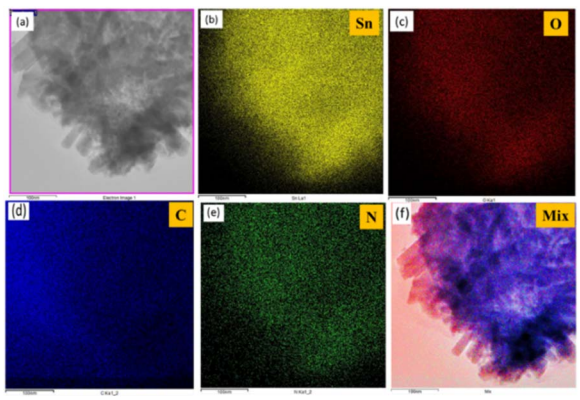

Fig. 10 FETEM-STEM-EDS elemental mapping images of 15 wt% g-C_3N_4@SnO_2 nanocomposite corresponding to (a) electron image, and elements, namely, (b) Sn, (c) O, (d) C, (e) N and (f) combined elemental mixture.

of g-C_3N_4, and thus the mix mode image (Fig. 10f) confirmed the g-C_3N_4@SnO_2 composite formation. Higher intensity of the colors allocated to Sn and O as compared to C and N was noticed which was tangible as amount of g-C_3N_4 was 15 wt% only.

BET surface area analysis

Fig. 11 displays the N_2 adsorption–desorption isotherms of the pristine g-C_3N_4, pristine SnO_2 and g-C_3N_4@SnO_2 composites prepared with g-C_3N_4 loading from 5 to 20 wt%. All the samples displayed type IV nitrogen adsorption–desorption isotherms maintaining type H_3 hysteresis loops (Fig. 11a). The detailed BET surface analysis results for the as-prepared pristine g-C_3N_4, pristine SnO_2 and g-C_3N_4@SnO_2 composite samples are summarized in Table 2.

The BET surface area of the pristine SnO_2 nanopowder was found to be 13.22 $m^2\ g^{-1}$, which showed that a notable increase in surface area occurred with increasing wt% loading of g-C_3N_4 due to the sheet-like structure of g-C_3N_4, which provided high surface area with corresponding values from 17.86 to 42.10 $m^2\ g^{-1}$. At moderate loading, g-C_3N_4 helps to disperse SnO_2

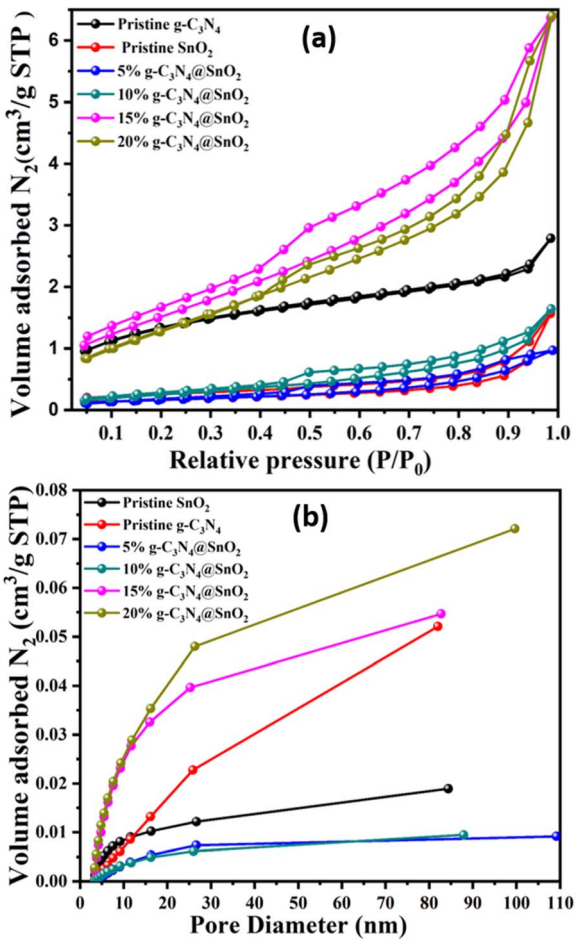

Fig. 11 BET surface area analysis of pristine g-C_3N_4, pristine SnO_2, and prepared g-C_3N_4@SnO_2 nanocomposites corresponding to (a) N_2 adsorption–desorption isotherms, and (b) BJH pore size distribution.

Table 2 BET surface area, total pore volume, BJH pore size, sensitivity, response and recovery times for pristine SnO_2, pristine g-C_3N_4 and g-C_3N_4@SnO_2 nanopowders

Sample		BET surface area (m^2 g^{-1})	Total pore volume (cm^3 g^{-1})	BJH pore size (nm)	Sensitivity (ohm/%RH)	Response time (s) (±3)	Recovery time (s) (±3)
Pristine SnO_2		13.22	0.0548	3.3736	0.45	63	75
Pristine g-C_3N_4		38.02	0.0352	3.3616	3.41	59	63
g-C_3N_4@SnO_2	5%	17.86	0.064	3.8128	4.92	30	40
	10%	18.27	0.083	3.2556	2.17	49	56
	15%	42.57	0.0097	3.3834	20.20	25	45
	20%	42.10	0.014	3.3546	9.20	50	38

particles and maintain accessible active sites. However, on increasing the g-C_3N_4 loading above 15 wt% on the SnO_2 surface, a slight reduction in the BET surface area was noted. Moreover, at higher loadings, the nanosheets tend to get stacked, agglomerate and wrap around SnO_2 particles, leading to pore blockage and reduced accessibility of active sites. Such over-coverage and structural compaction led to the observed reduction in surface area.

Humidity-sensing studies

Electrical resistance as a function of relative humidity for the sensors is depicted in Fig. 12, revealing the exponential decrease in the resistance of the prepared films with respect to the increase in the relative humidity for pristine SnO_2, pristine g-C_3N_4, and the 5 and 10 wt% g-C_3N_4@SnO_2 nanocomposites. On the contrary, almost linear performance was observed in case of the 15 and 20 wt% g-C_3N_4@SnO_2 nanocomposite. The ratio of the change in the resistance to the change in relative humidity (%RH) provided the value of sensitivity for all films (Table 2). It was observed that the sensor film corresponding to the 15 wt% g-C_3N_4@SnO_2 nanocomposite showed the highest response as compared to the other sensors.[43]

The response and recovery times for all the g-C_3N_4@SnO_2-based films are provided in Table 2 and Fig. 13. Primarily, the films were introduced to dry air conditions, explicitly at 20% RH. Upon switching to a humid environment enclosed within a sealed glass dome set at 80% RH, an instantaneous drop in film resistance was detected. Subsequently, upon switching the films back to the dry air environment (at 20% RH), the resistance was found to gradually recuperate to the initial value. To ascertain the consistency of the film's performance, three cycles of the above procedure were conducted to test the repeatability. As noted from the resistance transient curves, the best response and recovery times of 25 and 45 s were recorded for the 15 wt% g-C_3N_4@SnO_2 composite-based humidity sensor.

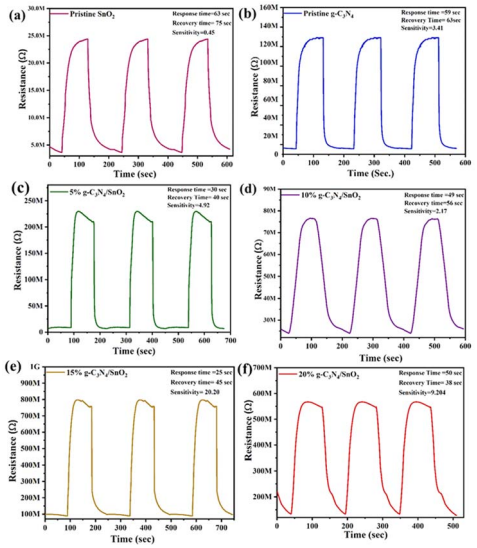

Fig. 13 Resistance transient curves of (a) pristine SnO_2, (b) pristine g-C_3N_4, and g-C_3N_4@SnO_2 nanocomposites with (c) 5 wt%, (d) 10 wt%, (e) 15 wt%, and (f) 20 wt% g-C_3N_4 loading, recorded under cyclic exposure to 20–80% RH.

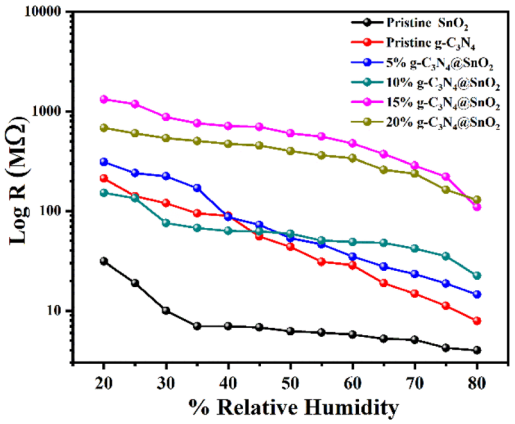

Fig. 12 Comparison of humidity-sensing analysis of pristine g-C_3N_4, pristine SnO_2, and prepared g-C_3N_4@SnO_2 composite powder-based sensors at various % relative humidities *vs.* log *R*.

Impedance response of 15 wt% g-C_3N_4@SnO_2 nanocomposite-based humidity sensor

The real and imaginary parts of impedance represent the DC resistivity and reactance of the material. Relaxation time (τ_Z) and location of a loss peak for frequency dependence of Im(Z) are correlated by eqn (1):[44]

$$\tau_Z = \frac{1}{2\pi f_{max}} \quad (1)$$

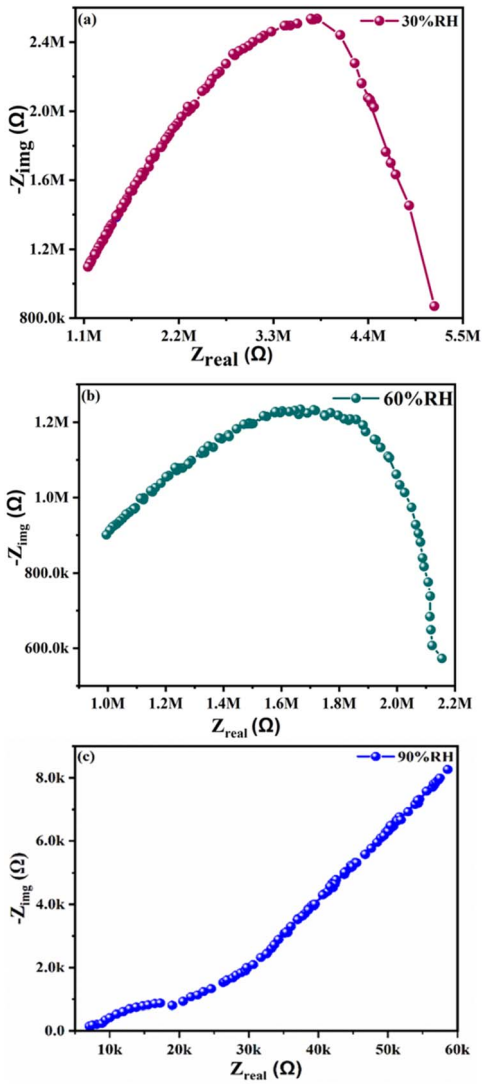

Fig. 14 Impendence measurement against (a) 30%, (b) 60% and (c) 90% relative humidity for the prepared 15% g-C_3N_4@SnO_2 nanocomposite humidity sensor.

where f_{max} represents the relaxation frequency for which the Im(Z) peak is observed. The centers of the semicircles obtained in the Nyquist plots of the 15% g-C_3N_4@SnO_2 nanocomposite-based humidity sensor were noted to be below the abscissa axis (Fig. 14a–c) indicating the occurrence of non-Debye relaxation processes and thus impedance spectroscopy is carried out by considering the constant phase elements (CPEs) for construction of an equivalent circuit.[45] The plotted values of resistance component were measured by LCR meter as a measure of sensor response.

For the 15% g-C_3N_4@SnO_2 nanocomposite-based humidity sensor, the measurement of charge transfer resistance (R_{ct}) represented the journey of an electron from one atom to another at the electrode and water vapour interface by assessing the diameter of the semicircle in the Nyquist plot (Fig. 14a–c). At 30%, 60% and 90% RH, the sensor exhibited a decrease in R_{ct} values (Table 3) corroborated by corresponding diminished semicircle diameters, suggesting a slower rate of electron transfer between the electrode surface and water vapour. This result is attributed to the gradual improvement of the material's electrical conductivity with increasing humidity levels.

Table 3 R_{ct} values at various relative humidities for prepared 15% g-C_3N_4@SnO_2 nanocomposite-based humidity sensor

Sr. no.	Relative humidity (%RH)	R_{ct} values (MΩ)
1	30	4.02
2	60	1.16
3	90	0.5

Mechanism of humidity sensing

The Grotthuss chain mechanism offers a methodical detailing of humidity sensing. In the basic concept of humidity sensing, the conductivity of hydrophilic metal oxide-based sensing layers is altered when interaction between their surface and water vapours takes place.[3]

Fig. 15 depicts a mechanism that explains physisorption of water molecules (Fig. 15a) followed by the splitting of water molecules owing to the inflated electrical fields. The enhanced sensing response of the 15 wt% g-C_3N_4@SnO_2 nanocomposite arises from a combination of efficient water adsorption, protonic conduction, and heterojunction-driven charge transfer. At this composition, the surface area and pore distribution provide favorable sites for physisorption of water molecules. Under the influence of localized electric fields, the adsorbed water undergoes dissociation to form H^+ and H_3O^+ ions, which migrate through the Grotthuss mechanism and significantly improve ionic conduction, thereby reducing resistance.[46,47] As humidity increases, adsorption of more water molecules on the surface takes place. The presence of a continuous water layer significantly increases the number of charge carriers, thereby reducing the overall electrical resistance. While air

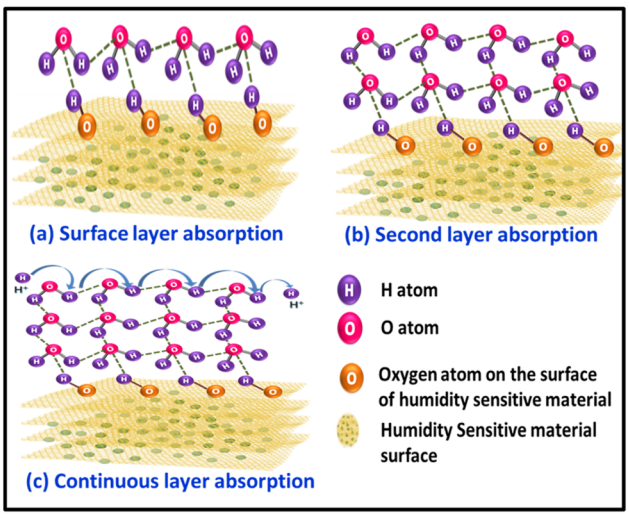

Fig. 15 Schematic for the humidity-sensing mechanism of the prepared g-C_3N_4@SnO_2 nanocomposites.

Table 4 Comparison of humidity-sensing performance of the prepared 15% g-C_3N_4@SnO_2 nanocomposite-based humidity sensor with available reports

Sr. No.	Material composition	Response time (s)	Recovery time (s)	Year	Ref.
1	ZnO–SnO_2	32	92	2019	49
2	RhAAm/SnO_2 nanocomposite	12	160	2021	50
3	Co-doped SnO_2/rGO	52	100	2022	51
4	SnO_2 thin film	84	576	2023	52
5	g-C_3N_4/GQDs nanocomposite	44	10	2023	53
6	SnO_2/Ti_3C_2Tx	14	49	2024	54
7	gC_3N_4/$Zn_{0.5}Ni_{0.5}Fe_{1.8}Mn_{0.2}O_4$/rGO	43	38	2025	55
8	**gC_3N_4@SnO_2**	**25**	**45**	**2025**	**Present work**

concentration differences may also contribute negligibly, the dominant factor is the enhanced surface conductivity due to interaction of water molecules with oxygen vacancies and hydroxyl groups present on the nanocomposite surface. The pore structure also facilitates capillary condensation, further enhancing water uptake and proton mobility.

In parallel, the intimate contact between g-C_3N_4 and SnO_2 establishes a heterojunction, since both are n-type semiconductors. The conduction band of g-C_3N_4 lies at a more negative potential than that of SnO_2, which drives electron transfer from g-C_3N_4 to SnO_2. This charge redistribution increases the interfacial potential barrier and promotes effective separation of photogenerated electrons and holes, consistent with previous reports on heterojunction-enhanced sensing.[48] At lower g-C_3N_4 contents, the interfacial coupling is insufficient and a limited number of water molecules are adsorbed onto the surface. While at higher contents, the excess coverage may hinder the exposure of SnO_2 active sites due to thicker g-C_3N_4 sheets. Thus, the 15 wt% g-C_3N_4@SnO_2 nanocomposite achieves the balance of optimal surface area for water adsorption, enhanced proton conduction *via* water dissociation, and efficient charge separation at the g-C_3N_4/SnO_2 heterojunction, resulting in the highest humidity-sensing performance. This synergistic effect, absent at lower or higher g-C_3N_4 loadings, accounts for the maximum sensitivity and fast response characteristics observed for 15 wt% g-C_3N_4@SnO_2 nanocomposite.

Table 4 provides a comparison of the humidity-sensing performance of the prepared 15% g-C_3N_4@SnO_2 nanocomposite against those of previously reported materials. The 15% g-C_3N_4@SnO_2 nanocomposite exhibits a clear advantage in terms of response speed, recovery, and sensitivity compared to the reported humidity sensors. While many SnO_2- or g-C_3N_4-based sensors deliver good performance, they often face drawbacks such as sluggish kinetics, restricted humidity ranges, or compromised stability. Our material overcomes these limitations by leveraging the synergistic interaction of g-C_3N_4 sheets with SnO_2 nanoparticles, which ensures abundant active sites and prevents pore blockage. Importantly, both components are low-cost and easily synthesized by scalable routes, making the sensor highly attractive for practical, energy-efficient, and economical humidity monitoring applications.

Conclusions

g-C_3N_4@SnO_2 nanocomposites were successfully synthesized through a combination of solvothermal and solid-state routes. XRD confirmed the tetragonal phase of SnO_2, while the presence of g-C_3N_4 could not be distinctly resolved due to peak overlap. Photoluminescence studies indicated defect-related vacancy states, while FESEM and FETEM analyses revealed the uniform distribution of SnO_2 nanoparticles on g-C_3N_4 sheets. The 15 wt% g-C_3N_4@SnO_2 composite exhibited the best humidity-sensing performance, with a sensitivity of 20.2 Ω/% RH, and fast response (25 s), and recovery (45 s) times. The enhanced sensing behavior can be attributed to heterojunction formation between SnO_2 and g-C_3N_4, which facilitates efficient charge separation and higher barrier potential.

Looking ahead, further optimization of g-C_3N_4 loading, defect engineering, and surface functionalization strategies could extend the sensing range and stability under varying environmental conditions. Integration of these composites into flexible substrates or miniaturized electronic platforms may pave the way for their application in wearable electronics, smart healthcare devices, and environmental monitoring. Thus, the reported g-C_3N_4@SnO_2 nanocomposite offers a promising pathway toward earth-abundant, low-cost, and next-generation humidity sensors.

Author contributions

The experiments have been performed by P. N. B. and planned by S. B. R., B. B. K and M. D. S. The data were analysed by P. N. B., M. D. S., and S. S. A, S.J. All the authors participated in writing the manuscript under the lead of S. B. R.

Conflicts of interest

There are no conflicts to declare.

Data availability

Supplementary information: the details of the Rietveld refined parameters used in the study, FTIR spectra of prepared pristine g-C_3N_4, SnO_2, and 5, 10, 15 and 20 wt% g-C_3N_4@SnO_2-composite powders, XPS survey scan spectra of prepared 15 wt%

g-C_3N_4@SnO_2 nanocomposite and FETEM images of prepared 15 wt% g-C_3N_4@SnO_2 nanostructures. See DOI: https://doi.org/10.1039/d5ra05966f.

Acknowledgements

Dr Priyanka Birla is thankful to the Department of Science and Technology, Ministry of Science and Technology, New Delhi for DST Women Scientist Fellowship (DST/WOSA/CS14/2021). Dr Priyanka is also thankful to Dr Kaustuv Bhattacharya, C-MET Pune for Rietveld refinement analysis.

References

1 T. Delipinar, A. Shafique, M. S. Gohar and M. K. Yapici, Fabrication and Materials Integration of Flexible Humidity Sensors for Emerging Applications, *ACS Omega*, 2021, **6**(13), 8744–8753, DOI: 10.1021/acsomega.0c06106.

2 D. Zhang, M. Wang, M. Tang, X. Song, X. Zhang, Z. Kang, X. Liu, J. Zhang and Q. Xue, Recent Progress of Diversiform Humidity Sensors Based on Versatile Nanomaterials and Their Prospective Applications, *Nano Res.*, 2023, **16**, 11938–11958, DOI: 10.1007/s12274-022-4917-y.

3 B. Arman Kuzubasoglu, Recent Studies on the Humidity Sensor: A Mini Review, *ACS Appl. Electron. Mater.*, 2022, **4**(10), 4797–4807, DOI: 10.1021/acsaelm.2c00721.

4 H. Tai, Z. Duan, Y. Wang, S. Wang and Y. Jiang, Paper-Based Sensors for Gas, Humidity, and Strain Detections: A Review, *ACS Appl. Mater. Interfaces*, 2020, **12**(28), 31037–31053, DOI: 10.1021/acsami.0c06435.

5 S. Ghosh, R. Ghosh, P. K. Guha and T. K. Bhattacharyya, Humidity Sensor Based on High Proton Conductivity of Graphene Oxide, *IEEE Trans. Nanotechnol.*, 2015, **14**(5), 931–937, DOI: 10.1109/TNANO.2015.2465859.

6 H. Chang, S. Feng, X. Qiu, H. Meng, G. Guo, X. He, Q. He, X. Yang, W. Ma, R. Kan, C. Fittschen and C. Li, Implementation of the toroidal absorption cell with multi-layer patterns by a single ring surface, *Opt. Lett.*, 2020, **45**, 5897–5900, DOI: 10.1364/OL.404198.

7 Y. Zhou, S. Fan, Z. Zhu, S. Su, D. Hou, H. Zhang and Y. Cao, Enabling high-sensitivity calorimetric flow sensor using vanadium dioxide phase-change material with predictable hysteretic behavior, *IEEE Trans. Electron Devices*, 2025, **72**(3), 1360–1367.

8 Z. H. Duan, Q. N. Zhao, C. Z. Li, S. Wang, Y. D. Jiang, Y. J. Zhang, B. H. Liu and H. L. Tai, Enhanced Positive Humidity Sensitive Behavior of P-Reduced Graphene Oxide Decorated with n-WS_2 Nanoparticles, *Rare Metals*, 2021, **40**(7), 1762–1767, DOI: 10.1007/s12598-020-01524-z.

9 M. Yang, M. Huang, Y. Li, Z. Feng, Y. Huang, H. Chen, Z. Xu, H. Liu and Y. Wang, Printing Assembly of Flexible Devices with Oxidation Stable MXene for High Performance Humidity Sensing Applications, *Sens. Actuators, B*, 2022, **364**, 131867, DOI: 10.1016/j.snb.2022.131867.

10 S. K. Kailasa, G. N. Vajubhai, J. R. Koduru, T. J. Park and C. M. Hussain, Recent Progress on the Modifications of Ultra-Small Perovskite Nanomaterials for Sensing Applications, *TrAC, Trends Anal. Chem.*, 2021, **144**, 116432, DOI: 10.1016/j.trac.2021.116432.

11 M. A. Najeeb, Z. Ahmad and R. A. Shakoor, Organic Thin-Film Capacitive and Resistive Humidity Sensors: A Focus Review, *Adv. Mater. Interfaces*, 2018, **5**(21), 1–19, DOI: 10.1002/admi.201800969.

12 S. Y. Park, J. E. Lee, Y. H. Kim, J. J. Kim, Y. S. Shim, S. Y. Kim, M. H. Lee and H. W. Jang, Room Temperature Humidity Sensors Based on RGO/MoS_2 Hybrid Composites Synthesized by Hydrothermal Method, *Sens. Actuators, B*, 2018, **258**, 775–782, DOI: 10.1016/j.snb.2017.11.176.

13 H. Dai, N. Feng, J. Li, J. Zhang and W. Li, Chemiresistive Humidity Sensor Based on Chitosan/Zinc Oxide/Single-Walled Carbon Nanotube Composite Film, *Sens. Actuators, B*, 2019, **283**, 786–792, DOI: 10.1016/j.snb.2018.12.056.

14 S. Kumar, K. K. Raina and T. Islam, Anodic Aluminium Oxide Based Humidity Sensor for Online Moisture Monitoring of Power Transformer, *Sens. Actuators, B*, 2021, **329**(September), 128908, DOI: 10.1016/j.snb.2020.128908.

15 J. Zhu, N. Zhang, Y. Yin, B. Xu, W. Zhang and C. Wang, High-Sensitivity and Low-Hysteresis $GONH_2$/Mesoporous SiO_2 Nanosphere-Fabric-Based Humidity Sensor for Respiratory Monitoring and Noncontact Sensing, *Adv. Mater. Interfaces*, 2022, **9**(1), 2101498, DOI: 10.1002/admi.202101498.

16 Z. Zhang, F. Li and Y. Zheng, Highly Sensitive Resistive Humidity Sensor Based on Strontium-Doped Lanthanum Ferrite Nanofibers, *Sens. Actuators, A*, 2023, **358**, 114435, DOI: 10.1016/j.sna.2023.114435.

17 B. Kalim, M. T. Ansar, Z. Ullah, S. K. Abbas, S. Riaz, S. A. Siddiqi and S. Atiq, CNTs/ZnO and CNTs/ZnO/Ag Multilayers Spray Coated on Cellulose Fiber for Use as an Efficient Humidity Sensor, *Ceram. Int.*, 2020, **46**(16), 25593–25597, DOI: 10.1016/j.ceramint.2020.07.031.

18 M. V. Arularasu, M. Harb, R. Vignesh, T. V. Rajendran and R. Sundaram, PVDF/ZnO Hybrid Nanocomposite Applied as a Resistive Humidity Sensor, *Surf. Interfaces*, 2020, **21**, 100780, DOI: 10.1016/j.surfin.2020.100780.

19 D. Toloman, A. Popa, M. Stan, C. Socaci, A. R. Biris, G. Katona, F. Tudorache, I. Petrila and F. Iacomi, Reduced Graphene Oxide Decorated with Fe Doped SnO_2 Nanoparticles for Humidity Sensor, *Appl. Surf. Sci.*, 2017, **402**, 410–417, DOI: 10.1016/j.apsusc.2017.01.064.

20 M. Panday, G. K. Upadhyay and L. P. Purohit, Sb Incorporated SnO_2 Nanostructured Thin Films for CO_2 Gas Sensing and Humidity Sensing Applications, *J. Alloys Compd.*, 2022, **904**, 164053, DOI: 10.1016/j.jallcom.2022.164053.

21 H. Jeong, Y. Noh and D. Lee, Highly Stable and Sensitive Resistive Flexible Humidity Sensors by Means of Roll-to-Roll Printed Electrodes and Flower-like TiO_2 Nanostructures, *Ceram. Int.*, 2019, **45**(1), 985–992, DOI: 10.1016/j.ceramint.2018.09.276.

22 S. Mallick, Z. Ahmad, F. Touati, J. Bhadra, R. A. Shakoor and N. J. Al-Thani, PLA-TiO_2 Nanocomposites: Thermal, Morphological, Structural, and Humidity Sensing Properties, *Ceram. Int.*, 2018, **44**(14), 16507–16513, DOI: 10.1016/j.ceramint.2018.06.068.

23 K. Malook, H. Khan, M. Ali and Ihsan-Ul-Haque, Investigation of Room Temperature Humidity Sensing Performance of Mesoporous CuO Particles, *Mater. Sci. Semicond. Process.*, 2020, **113**(December 2019), 105021, DOI: 10.1016/j.mssp.2020.105021.

24 M. Saquib, S. Shiraj, R. Nayak, A. Nirmale and M. Selvakumar, Synthesis and Fabrication of Graphite/WO_3 Nanocomposite-Based Screen-Printed Flexible Humidity Sensor, *J. Electron. Mater.*, 2023, **52**(6), 4226–4238, DOI: 10.1007/s11664-023-10404-y.

25 A. Kumar, G. Gupta, K. Bapna and D. D. Shivagan, Semiconductor-Metal-Oxide-Based Nano-Composites for Humidity Sensing Applications, *Mater. Res. Bull.*, 2023, **158**, 112053, DOI: 10.1016/j.materresbull.2022.112053.

26 J. Zhu, P. Xiao, H. Li and S. A. C. Carabineiro, Graphitic Carbon Nitride: Synthesis, Properties, and Applications in Catalysis, *ACS Appl. Mater. Interfaces*, 2014, **6**(19), 16449–16465, DOI: 10.1021/am502925j.

27 M. Morsy, I. Gomaa, M. M. Mokhtar, H. ElHaes and M. Ibrahim, Design and Implementation of Humidity Sensor Based on Carbon Nitride Modified with Graphene Quantum Dots, *Sci. Rep.*, 2023, **13**(1), 1–18, DOI: 10.1038/s41598-023-29960-8.

28 W. Meng, S. Wu, X. Wang and D. Zhang, High-Sensitivity Resistive Humidity Sensor Based on Graphitic Carbon Nitride Nanosheets and Its Application, *Sens. Actuators, B*, 2020, **315**(December 2019), 128058, DOI: 10.1016/j.snb.2020.128058.

29 S. Das and V. Jayaraman, SnO_2: A Comprehensive Review on Structures and Gas Sensors, *Prog. Mater. Sci.*, 2014, **66**, 112–255, DOI: 10.1016/j.pmatsci.2014.06.003.

30 Y. Zhang, J. Liu, X. Chu, S. Liang and L. Kong, Preparation of g–C_3N_4–SnO_2 Composites for Application as Acetic Acid Sensor, *J. Alloys Compd.*, 2020, **832**, 153355, DOI: 10.1016/j.jallcom.2019.153355.

31 V. K. Tomer and S. Duhan, A Facile Nanocasting Synthesis of Mesoporous Ag-Doped SnO_2 Nanostructures with Enhanced Humidity Sensing Performance, *Sens. Actuators, B*, 2016, **223**, 750–760, DOI: 10.1016/j.snb.2015.09.139.

32 X. Song, Q. Qi, T. Zhang and C. Wang, A Humidity Sensor Based on KCl-Doped SnO_2 Nanofibers, *Sens. Actuators, B*, 2009, **138**(1), 368–373, DOI: 10.1016/j.snb.2009.02.027.

33 N. Rahman, J. Yang, Zulfiqar, M. Sohail, R. Khan, A. Iqbal, C. Maouche, A. A. Khan, M. Husain, S. A. Khattak, S. N. Khan and A. Khan, Insight into Metallic Oxide Semiconductor (SnO_2, ZnO, CuO, α-Fe_2O_3, WO_3)-Carbon Nitride (g-C_3N_4) Heterojunction for Gas Sensing Application, *Sens. Actuators, A*, 2021, **332**, 113128, DOI: 10.1016/j.sna.2021.113128.

34 J. Cao, C. Qin, Y. Wang, H. Zhang, B. Zhang, Y. Gong, X. Wang, G. Sun, H. Bala and Z. Zhang, Synthesis of g-C_3N_4 Nanosheet Modified SnO2 Composites with Improved Performance for Ethanol Gas Sensing, *RSC Adv.*, 2017, **7**(41), 25504–25511, DOI: 10.1039/c7ra01901g.

35 H. Wu, S. Yu, Y. Wang, J. Han, L. Wang, N. Song, H. Dong and C. Li, A Facile One-Step Strategy to Construct 0D/2D SnO_2/g-C_3N_4 Heterojunction Photocatalyst for High-Efficiency Hydrogen Production Performance from Water Splitting, *Int. J. Hydrogen Energy*, 2020, **45**(55), 30142–30152, DOI: 10.1016/j.ijhydene.2020.08.112.

36 Y. Zang, L. Li, X. Li, R. Lin and G. Li, Synergistic Collaboration of g-C_3N_4/SnO_2 Composites for Enhanced Visible-Light Photocatalytic Activity, *Chem. Eng. J.*, 2014, **246**, 277–286, DOI: 10.1016/j.cej.2014.02.068.

37 V. K. Tomer and S. Duhan, A Facile Nanocasting Synthesis of Mesoporous Ag-Doped SnO_2 Nanostructures with Enhanced Humidity Sensing Performance, *Sens. Actuators, B*, 2016, **223**, 750–760, DOI: 10.1016/J.SNB.2015.09.139.

38 K. Zhu, Y. Lv, J. Liu, W. Wang, C. Wang, S. Li, P. Wang, M. Zhang, A. Meng and Z. Li, Facile Fabrication of g-C_3N_4/SnO_2 Composites and Ball Milling Treatment for Enhanced Photocatalytic Performance, *J. Alloys Compd.*, 2019, **802**, 13–18, DOI: 10.1016/j.jallcom.2019.06.193.

39 Y. Cheng, H. Xie, F. Yu, J. Zhang, Y. Wang, X. Luo, B. Shi and B. Liu, Facile Fabrication of Three-Dimensional Porous Carbon Embedded with SnO_2 Nanoparticles as a High-Performance Anode for Lithium-Ion Battery, *Ionics*, 2021, **27**(10), 4143–4151, DOI: 10.1007/s11581-021-04177-9.

40 A. Mohammad, M. E. Khan, M. R. Karim, M. H. Cho and T. Yoon, Ag-Modified SnO_2-Graphitic-Carbon Nitride Nanostructures for Electrochemical Sensor Applications, *Ceram. Int.*, 2021, **47**(16), 23578–23589, DOI: 10.1016/j.ceramint.2021.05.076.

41 W. Guo, L. Huang, J. Zhang, Y. He and W. Zeng, Ni-Doped SnO_2/g-C_3N_4 Nanocomposite with Enhanced Gas Sensing Performance for the Eff; Ective Detection of Acetone in Diabetes Diagnosis, *Sens. Actuators, B*, 2021, **334**, 129666, DOI: 10.1016/j.snb.2021.129666.

42 A. Ahmed, M. N. Siddique, U. Alam, T. Ali and P. Tripathi, Improved photocatalytic activity of Sr doped SnO_2 nanoparticles: A role of oxygen vacancy, *Appl. Surf. Sci.*, 2019, **463**, 976–985, DOI: 10.1016/j.apsusc.2018.08.182.

43 S. Atkare, S. Hambir, S. Jagtap, A. Adhikari, S. K. Singh and R. Patel, Role of Polyaniline/Molybdenum Trioxide Nanocomposites in Tuning the Characteristics of Humidity Sensors, *Polym. Adv. Technol.*, 2023, **34**(8), 2585–2596, DOI: 10.1002/pat.6074.

44 K. Mistewicz, A. Starczewska, M. Jesionek, M. Nowak, M. Kozioł and D. Stróż, Humidity Dependent Impedance Characteristics of SbSeI Nanowires, *Appl. Surf. Sci.*, 2020, **513**(December 2019), 145859, DOI: 10.1016/j.apsusc.2020.145859.

45 B. Arman Kuzubasoglu, Recent studies on the humidity sensor: A mini review, *ACS Appl. Electron. Mater.*, 2022, **4**(10), 4797–4807, DOI: 10.1021/acsaelm.2c00721.

46 A. Šutka and K. A. Gross, Spinel Ferrite Oxide Semiconductor Gas Sensors, *Sens. Actuators, B*, 2016, **222**, 95–105, DOI: 10.1016/j.snb.2015.08.027.

47 R. Zhao, Z. Wang, T. Zou, Z. Wang, Y. Yang, X. Xing and Y. Wang, Synthesis and Enhanced Sensing Performance of g-C_3N_4/SnO_2 Composites toward Isopropanol, *Chem. Lett.*, 2018, **47**(7), 881–882, DOI: 10.1246/cl.180296.

48 S. Kunchakara, A. Ratan, M. Dutt, J. Shah, R. K. Kotnala and V. Singh, Impedimetric Humidity Sensing Studies of Ag

Doped MCM-41 Mesoporous Silica Coated on Silver Sputtered Interdigitated Electrodes, *J. Phys. Chem. Solids*, 2020, **145**, 109531, DOI: 10.1016/j.jpcs.2020.109531.

49 M. Velumani, S. R. Meher and Z. C. Alex, Composite metal oxide thin film based impedometric humidity sensors, *Sens. Actuators, B*, 2019, **301**, 127084, DOI: 10.1016/j.snb.2019.127084.

50 L. K. Gupta, K. Kumar, B. C. Yadav, T. P. Yadav, G. I. Dzhardimalieva, I. E. Uflyand and Shripal, Comparative study on humidity sensing abilities of synthesized mono and poly rhodium acryl amide tin oxide (RhAAm/SnO_2) nanocomposites, *Sens. Actuators, A*, 2021, **330**, 112839, DOI: 10.1016/j.sna.2021.112839.

51 A. I. Madbouly, M. Morsy and R. F. Alnahdi, Microwave-assisted synthesis of Co-doped SnO_2/rGO for indoor humidity monitoring, *Ceram. Int.*, 2022, **48**(10), 13604–13614, DOI: 10.1016/j.ceramint.2022.01.240.

52 A. Kumar, P. Kumari, M. S. Kumar, G. Gupta, D. D. Shivagan and K. Bapna, SnO_2 nanostructured thin film as humidity sensor and its application in breath monitoring, *Ceram. Int.*, 2023, **49**(15), 24911–24921, DOI: 10.1016/j.ceramint.2023.05.020.

53 M. Morsy, I. Gomaa, M. M. Mokhtar, et al., Design and implementation of humidity sensor based on carbon nitride modified with graphene quantum dots, *Sci. Rep.*, 2023, **13**, 2891, DOI: 10.1038/s41598-023-29960-8.

54 S.-F. Tseng, S.-J. Cheng, W.-T. Hsiao, S.-H. Hsu and C.-C. Kuo, High-performance humidity sensors based on SnO_2/$Ti_3C_2T_x$ nanocomposites coated on porous graphene electrodes, *Ceram. Int.*, 2024, **50**(21), 43728–43737, DOI: 10.1016/j.ceramint.2024.08.224.

55 M. Rahman, M. L. Rahman, B. Biswas, M. F. Ahmed, M. A. A. Shaikh, S. A. Jahan and N. Sharmin, Fabrication of novel ternary g-C_3N_4/$Zn_{0.5}Ni_{0.5}Fe_{1.8}Mn_{0.2}O_4$/rGO hybrid nanocomposites for humidity sensing, *Nanoscale Adv.*, 2025, **7**, 1489–1504, DOI: 10.1039/D4NA00579A.